Appendix A

Blonder-Tinkham-Klapwijk Formalism

The Bogoliubov–de Gennes (BdG) equations generalize the BCS formalism to treat superconductors with spatially varying pairing strength $\Delta(x)$, chemical potential $\mu(x)$, and Hartree potential $V(x)$. The excitation described by the operator $\gamma^{\dagger}_{e,k_+\uparrow} = u_{k_+} c^{\dagger}_{k_+\uparrow} - v_{k_+} S^{\dagger} c_{-k_+\downarrow}$ with charge e is represented as a two-element column vector

$$\psi_k = \begin{bmatrix} u_k(x.t) \\ v_k(x,t) \end{bmatrix}, \tag{A.1}$$

where u_k and v_k satisfy the equations

$$\begin{cases} \left[-\frac{\hbar^2}{2m}\nabla^2 + V(x) - \mu(x)\right] u_k(x,t) + \Delta(x) v_k(x,t) &= i\hbar \frac{\partial u_k(x,t)}{\partial t} \\ -\left[-\frac{\hbar^2}{2m}\nabla^2 + V(x) - \mu(x)\right] v_k(x,t) + \Delta^*(x) u_k(x,t) &= i\hbar \frac{\partial v_k(x,t)}{\partial t}. \end{cases} \tag{A.2}$$

Deep in the superconducting electrode where $\Delta(x)$, $\mu(x)$, and $V(x)$ are constants, the solutions to (A.2) are time-independent plane waves. Let $u_k(x,t) = u_k e^{ikx - iE_k t/\hbar}$ and $v_k(x,t) = v_k e^{ikx - iE_k t/\hbar}$. For $V(x) = 0$, (A.2) reads

$$\begin{cases} E_k u_k &= \left[-\frac{\hbar^2 k^2}{2m} - \mu\right] u_k + \Delta\, v_k \\ E_k v_k &= -\left[-\frac{\hbar^2 k^2}{2m} - \mu\right] v_k + \Delta\, u_k. \end{cases} \tag{A.3}$$

For each energy E_k, there are 4 corresponding k values, $\pm k_\pm$, where

$$\frac{\hbar^2 k_\pm^2}{2m} = \mu \pm \sqrt{E_k^2 - |\Delta|^2}. \tag{A.4}$$

In Eq. (A.4), k_+ labels the electron-like quasiparticles, and k_- labels the hole-like quasiparticles, since

$$\begin{cases} u_{k_+}^2 &= \frac{1}{2}(1 + \frac{\sqrt{E_k^2-\Delta^2}}{E_k}) \equiv u_{k0}^2 > \frac{1}{2} \\ v_{k_+}^2 &= \frac{1}{2}(1 - \frac{\sqrt{E_k^2-\Delta^2}}{E_k}) \equiv v_{k0}^2 < \frac{1}{2} \end{cases} \tag{A.5}$$

$$\begin{cases} u_{k_-}^2 &= \frac{1}{2}(1 - \frac{\sqrt{E_k^2-\Delta^2}}{E_k}) = v_{k0}^2 < \frac{1}{2} \\ v_{k_-}^2 &= \frac{1}{2}(1 + \frac{\sqrt{E_k^2-\Delta^2}}{E_k}) = u_{k0}^2 > \frac{1}{2}. \end{cases} \tag{A.6}$$

The corresponding wavefunctions are

$$\psi_{\pm k_\pm}^S = \begin{bmatrix} u_{\pm k_\pm}(x) e^{-iE_k t/\hbar} \\ v_{\pm k_\pm}(x) e^{-iE_k t/\hbar} \end{bmatrix} = e^{\pm i k_\pm x} \begin{bmatrix} \sqrt{\frac{1}{2}(1 \pm \frac{\sqrt{E_k^2-\Delta^2}}{E_k})} \\ \sqrt{\frac{1}{2}(1 \mp \frac{\sqrt{E_k^2-\Delta^2}}{E_k})} \end{bmatrix} e^{-iE_k t/\hbar}. \tag{A.7}$$

Similarly, in the normal electrode sufficiently far away from the interface, $V(x) = \Delta(x) = 0$, and $\frac{\hbar^2 k_\pm^2}{2m} = \mu \pm E_k$. The wavefunctions are

$$\psi_{\pm k_+}^N = \begin{bmatrix} u_{\pm k_+}(x) e^{-iE_k t/\hbar} \\ v_{\pm k_+}(x) e^{-iE_k t/\hbar} \end{bmatrix} = e^{\pm i k_+ x} \begin{bmatrix} 1 \\ 0 \end{bmatrix} e^{-iE_k t/\hbar} \text{ (electron-branch)} \tag{A.8}$$

$$\psi_{\pm k_-}^N = \begin{bmatrix} u_{\pm k_-}(x) e^{-iE_k t/\hbar} \\ v_{\pm k_-}(x) e^{-iE_k t/\hbar} \end{bmatrix} = e^{\pm i k_- x} \begin{bmatrix} 0 \\ 1 \end{bmatrix} e^{-iE_k t/\hbar} \text{ (hole-branch)}, \tag{A.9}$$

where

$$E_k = \begin{cases} \frac{\hbar^2 k_+^2}{2m} - \mu, & (|k_+| > k_f) \\ \mu - \frac{\hbar^2 k_-^2}{2m}, & (|k_-| < k_f). \end{cases} \tag{A.10}$$

To model the N-S interface, BTK follows Demers and Griffin [284, 285] and represents the interface by a repulsive delta-function potential $V(x) = H\delta(0)$. We restrict our discussion to elastic

tunneling processes. The constraint that, for an incident particle with a positive group velocity ($dE_k/\hbar dk$) only transmitted particles with positive group velocities and reflected ones with negative group velocities can be generated, narrows down the number of allowed processes to four [Fig. A.1]. Given an incident electron from the normal electrode, it can be Andreev-reflected as an hole, normal-reflected as an electron, transmitted as an electron-like quasiparticle, or transmitted as a hole-like quasiparticle. Therefore, for electrons traveling from N to S, the wavefunctions of the normal and superconducting electrodes consist of

$$\begin{aligned}
\psi^N_{\rm inc} &= \begin{bmatrix} 1 \\ 0 \end{bmatrix} e^{ik_+x}, \\
\psi^N_{\rm refl} &= a \begin{bmatrix} 0 \\ 1 \end{bmatrix} e^{ik_-x} + b \begin{bmatrix} 1 \\ 0 \end{bmatrix} e^{-ik_+x}, \\
\psi^S_{\rm trans} &= c \begin{bmatrix} u^2_{k0} \\ v^2_{k0} \end{bmatrix} e^{ik_+x} + d \begin{bmatrix} v^2_{k0} \\ u^2_{k0} \end{bmatrix} e^{-ik_-x},
\end{aligned} \tag{A.11}$$

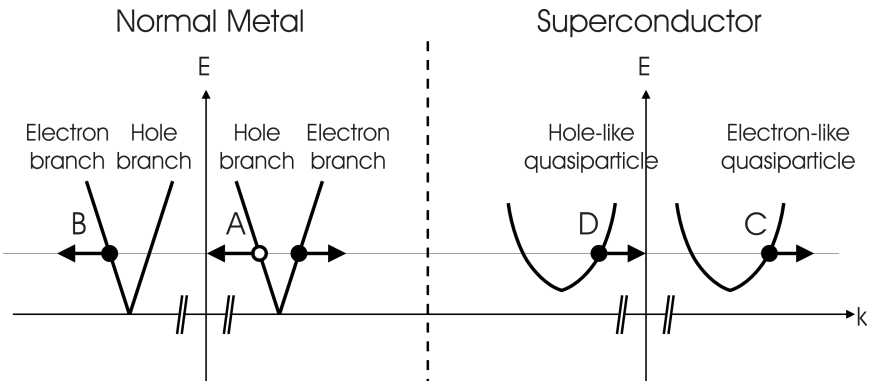

Figure A.1: Schematic diagram of energy vs. momentum at N-S interface modified from Fig. 4 in [122]. The open circles denote holes, and closed circles electrons, and the arrows point in the direction of the group velocity. The figure illustrates the four allowed processes for an incident electron at (0): the Andreev-reflected hole (A), the normal-reflected electron (B), the transmitted electron-like quasiparticle (C) and the transmitted hole-like quasiparticle (D).

Apply the following boundary conditions to solve for the prefactors $a - d$: (1) The wavefunction values are continuous at the interface $x = 0$: $\psi^N(0) = \psi^S(0) = \psi(0)$. (2) The derivative of the wavefunctions satisfies $\frac{\hbar}{2m}\frac{d\psi^S(0)}{dx} - \frac{\hbar}{2m}\frac{d\psi^N(0)}{dx} = H\psi(0)$. We obtain the probability current for

Andreev refleciton $A(E)$ and that for normal reflection $B(E)$

$$\left.\begin{array}{rcccl} A(E) & = & |a(E)|^2 & = & \frac{u_0^2 v_0^2}{\gamma^2} \\ B(E) & = & |b(E)|^2 & = & \frac{(u_0^2-v_0^2)^2 Z^2(1+Z^2)}{\gamma^2} \end{array}\right\} (E > \Delta) \tag{A.12}$$

$$\left.\begin{array}{rcccl} A(E) & = & |a(E)|^2 & = & \frac{\Delta^2}{E^2+(\Delta^2-E^2)(1+2Z^2)^2} \\ B(E) & = & |b(E)|^2 & = & 1-A \end{array}\right\} (E < \Delta), \tag{A.13}$$

where the dimensionless barrier height $Z = mH/\hbar^2 k_f$, $\gamma = u_0^2 + (u_0^2 - v_0^2)Z^2$, and the subscript k has been dropped.

Consequently, when a bias voltage is applied, the total current flowing from the normal to the superconducting electrode is

$$I(V) \propto N(0) \int_{-\infty}^{\infty} [f(E-eV) - f(E)] \left[1 + |a(E)|^2 - |b(E)|^2\right] dE. \tag{A.14}$$

Equation (A.14) shows that Andreev reflection increases the current transmission while the normal reflection reduces tunneling current. The zero-temperature differential tunneling conductance $\frac{dI}{dV}(V) \propto \left[1 + |a(E)|^2 - |b(E)|^2\right]$ versus bias voltage V for a number of barrier heights Z is plotted in Fig. A.2. In the limit of zero-barrier height, the conductance within the superconducting gap nearly doubles because most of the incident electrons are Andreev-reflected and the transmitted electron pairs across the interface carries double the amount of charge of the incident electrons. On the contrary, in the high-barrier limit, the result given by the BTK formalism is essentially the same as that of the transfer Hamiltonian (*cf.* the conductance plot for $Z = 5.0$ in Fig. A.2).

We remark that the BTK theory is a mean-field theory, for it is based on the Bogoliubov–de Gennes equation. Therefore, residual interactions, such as quasiparticle scattering and quasiparticle coupling with the bosonic modes of the system, are not accounted for. The original BTK theory describes the tunneling process between a normal metal and a conventional s-wave superconductor. To investigate the consequence of unconventional pairing symmetries, in particular the d-wave pairing

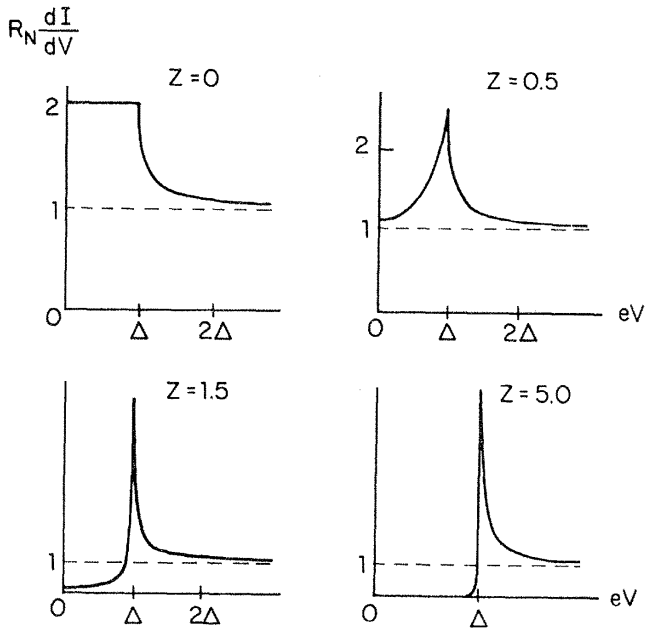

Figure A.2: Differential tunneling conductance vs. bias voltage for various normalized barrier heights Z at zero temperature. Figure taken from [122].

in the hole-doped cuprates, we resort to the generalized BTK formalism developed by Tanaka and Kashiwaya [124, 125] introduced in §2.2.1.

Appendix B

Tip Preparation, Piezo Calibration, and Thermal Drifting

B.1 Tip preparation

The STM tips for this thesis study were made of 15 mil Pt/Ir (.85/.15) wires. A number of tip preparation procedures were trialed to optimize the tip quality. Different tips suit different samples. To image a flat sample, such as that of a highly ordered pyrolytic graphite (HOPG), a simple mechanically cut Pt/Ir tip can produce good atomic images as long as the apex of the tip is free of undesirable atoms or molecules. Thus, before calibrating the piezo-tube scanner against HOPG, we cleaned the mechanically sheared tips in saturated hydrochloric acid (HCl) to remove unwanted material. A exemplary image of a tip after cleaning is shown in Fig. B.1(a).

To image rough surfaces, tips with a sharp and well-defined shape are preferable. Electrochemical etching has been proven to yield sharp tungsten tips. For inert metals, such as the Pt/Ir wires, well-controlled etching can be tricky. We had several trials on various etching methods, including the micro-polishing technique [286], before we successfully produced a sharp tip with good aspect ratio following the three-step recipe given by [287] (Fig. B.1(b)).

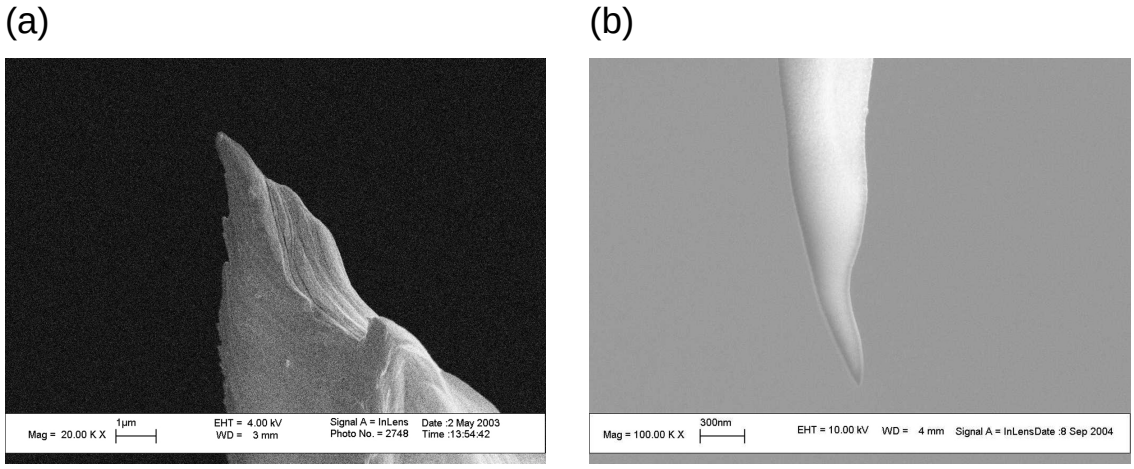

Figure B.1: (a) SEM image of a mechanically cut Pt/Ir tip after HCl cleaning. (b) SEM image of a tapered tip after the three-step electrochemical etching.

B.2 Piezo calibration and HOPG images

To calibrate the shear-piezos of the coarse approach motor, a Michaelson interferometer is set up to measure both their polarization and displacement coefficient. We use type EBL #2 piezos purchased from Staveley sensor whose shear-coefficient ranges from 5 Å/V to 10 Å/V. Among all piezos, we pick those with similar coefficients ($\sim 7-8$ Å/V) for the STM head construction.

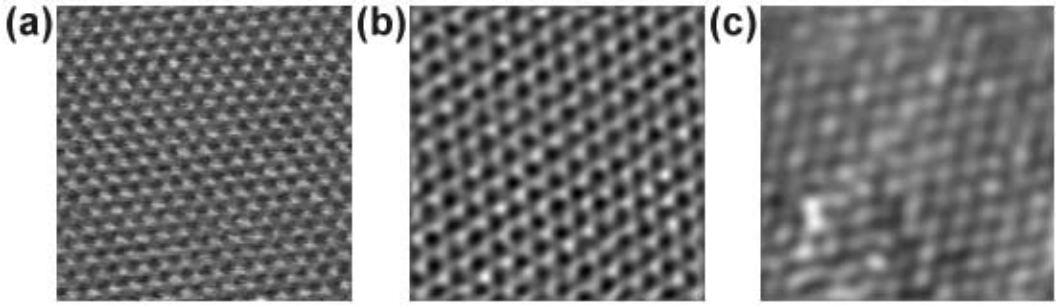

Figure B.2: (a) STM topographic images of highly ordered pyrolytic graphite at 295K (37 Å$\times$37 Å), (b) at 77K (29 Å $\times$ 29 Å), and (c) at 4.2K (30 Å $\times$ 30 Å).

A 0.125″ O.D., 0.6″ long, 20 mil thick EBL#2 tube serves as our STM scanner. To calibrate the piezo-tube scanner, atomic-resolved images on HOPG are taken at 295K, 77K, and 4.2K (Fig. B.2). Knowing the carbon-carbon separation in graphite, we then extract the piezo coefficient for lateral scanning and plot them in Fig. B.3. Notice that the coefficient decreases linearly with decreasing temperatures. Therefore, at any intermediate temperatures, a simple linear interpolation is sufficient

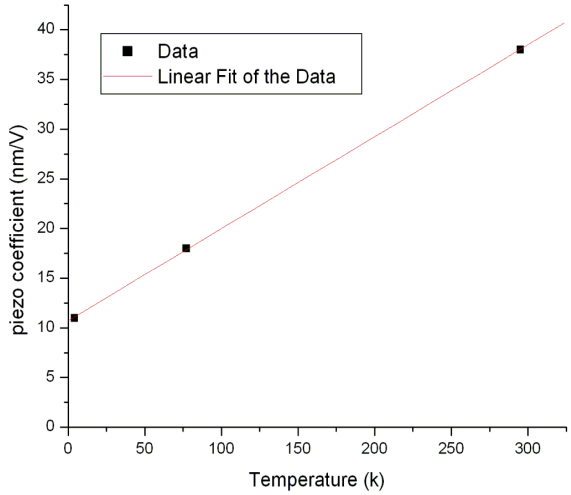

Figure B.3: The temperature dependence of the coefficient of the STM piezo-tube scanner is linear.

to rescale the STM images.

B.3 Thermal drifting calibration and gold images

It is preferable that we can return to the same location under study after withdrawing the tip for helium transfer. Figure B.4 demonstrates that the STM head is capable of retrieving the feature of interest upon re-approach. we find that the biggest source of drifting upon re-approach comes from the misalignment between the vertical axis of the tip holder and the normal direction of the sample holder. We reduce this problem by restricting the servo range to make sure that the piezo tube is under roughly the same amount of extension every time the tip reaches tunneling range. Figure B.4 shows that this trick helps to reduce the undesirable displacement to less than 10 Å.

In order to perform scanning tunneling spectroscopy at elevated temperatures, it is necessary to make sure that the thermal drifting of the tip relative to the sample can be compensated by the piezo tube scanner. We present the STM images of gold taken at the temperature range $10 - 35$ K with a 5 K interval, which demonstrate that the STM head is capable of tracing the feature of interest upon the increase of temperatures [Fig. B.5]. The origin of the image taken at 15 K and 35 K have been shifted so as to demonstrate the ability of the STM to compensate for thermal drifting. The estimated drifting between 10 K and 15 K is $\sim$ (90 Å, 110 Å), between 15

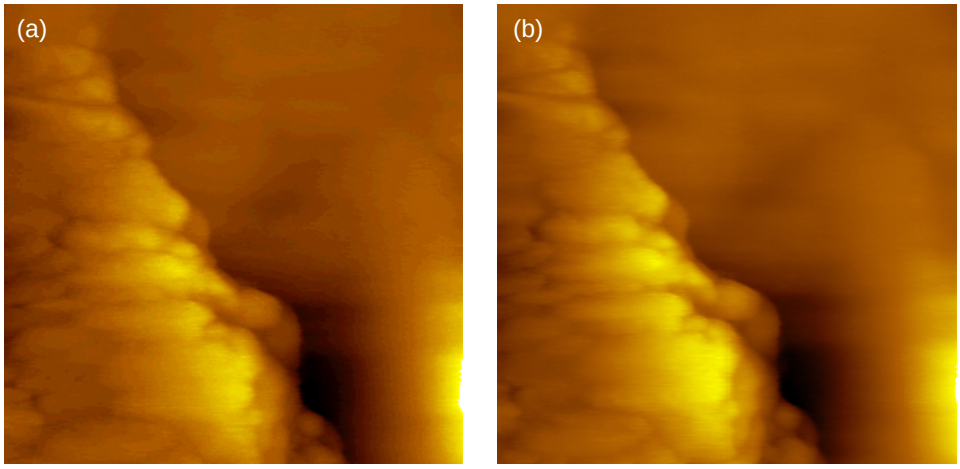

Figure B.4: Gold images (200 Å × 200 Å) taken at 10 K (a) before and (b) after we withdraw the tip for ~ 50 μm and re-approach. The displacement between frames is no more than 10 Å.

K and 20 K $\sim (110\text{ Å}, 60\text{ Å})$, between 20 K and 25 K $\sim (155\text{ Å}, -65\text{ Å})$, between 25 K and 30 K $\sim (145\text{ Å}, -215\text{ Å})$, and between 30 K and 35 K $\sim (135\text{ Å}, -110\text{ Å})$, where (x, y) denotes the displacement along the x- and y-axes respectively. We note that the piezo coefficient of the tube scanner does not change much with the sample temperatures, indicative of good thermal isolation between the sample stage and the rest of the STM probe. During each temperature increment, the STM tip is retracted out of the tunneling range by ~ 500 nm before ramping up the temperature in order to avoid crashing the tip onto the sample. In general, each temperature increment takes about half $15 - 30$ minutes to reach thermal equilibrium and to fully relax the piezo tube.

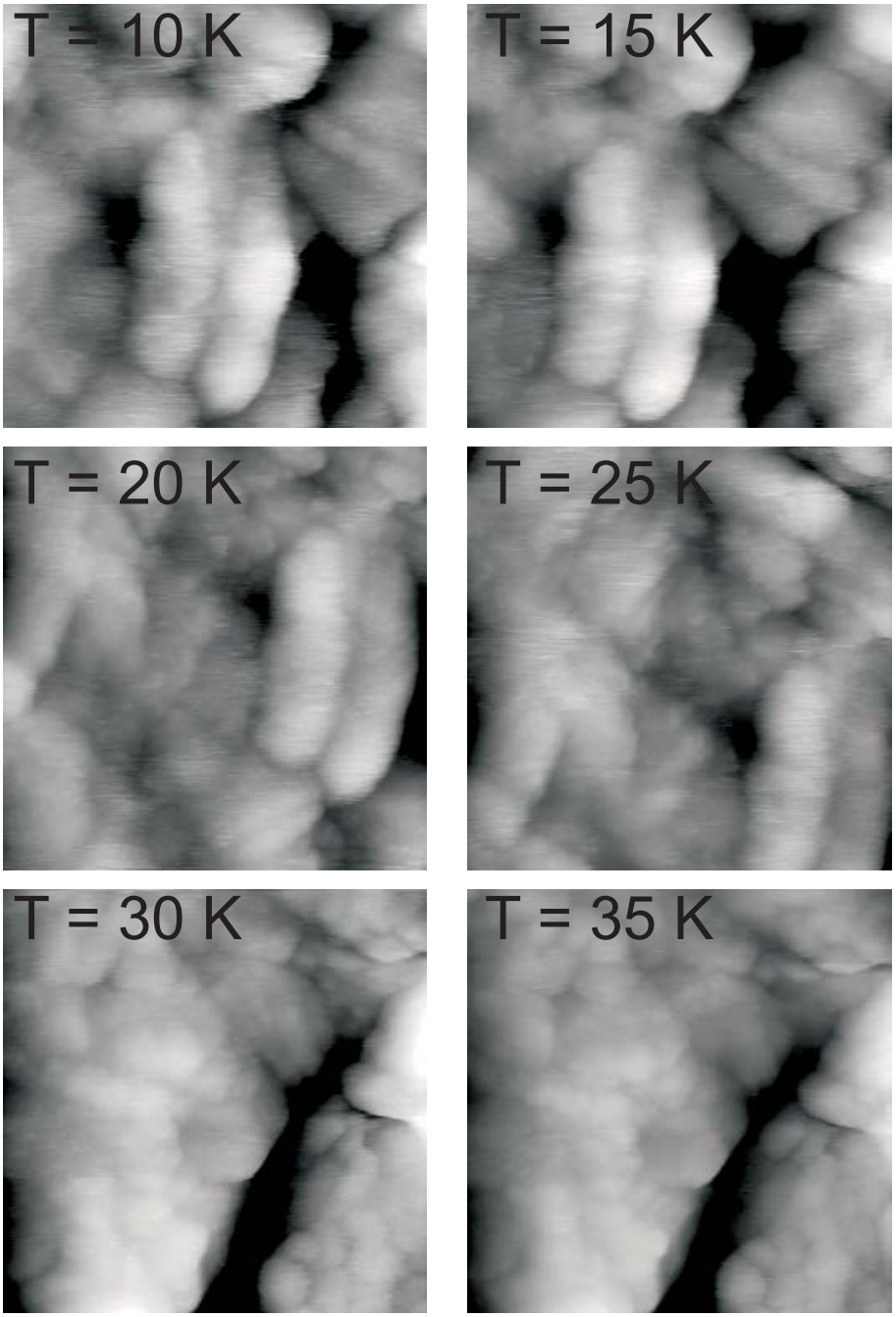

Figure B.5: STM topographic images of gold (400 Å × 400 Å) taken at various temperatures to calibrate for thermal drifting.

Appendix C

Modeling the STS data in the presence of impurities

To extract information encoded in the the spatially resolved scanning tunneling spectroscopy, we recall that, for tunneling into a superconductor, the tunneling current is given by

$$I(V) \propto \int_{-\infty}^{\infty} d\xi \, |D|^2 \, [f(\xi) - f(\xi + eV)] \, N_S(\xi + eV), \tag{C.1}$$

where $N_S(\xi)$ is the density of states of the superconducting electrode, and Δ is the energy gap of the superconductor. Assuming D varies slightly with energy, the tunneling conductance $\frac{dI}{dV}(\vec{r}, V)$ measures the local density of states (LDOS) directly in the low temperature limit:

$$\frac{dI}{dV}(\vec{r}, V) \quad \propto \quad |D|^2 \, N_S \, (\vec{r}, eV) \, . \tag{C.2}$$

The LDOS is related to the retarded Green's function through

$$N_S \, (\vec{r}, \omega) = -\frac{1}{\pi} \, \mathrm{Im} \, [G^{\mathrm{ret}}(\vec{r}, \vec{r}, \omega)], \tag{C.3}$$

where $G^{\mathrm{ret}}(\vec{r}, \vec{r}, \omega)$ is the Fourier transform of $G^{\mathrm{ret}}(\vec{r}, \vec{r}, t)$. Let H be the total Hamiltonian of the system and $\psi_{\mathbf{q}}(\vec{r})$ the single-particle eigenstates. Then $G^{\mathrm{ret}}(\vec{r}, \vec{r}, t)$ is defined as:

$$G^{\mathrm{ret}}(\vec{r}, \vec{r}, t) = -i\theta(t) \sum_q \left\langle \vec{r} \right| e^{-i\hat{H}t/\hbar} \left| \psi_{\mathbf{q}} \right\rangle \langle \psi_{\mathbf{q}} | \vec{r} \rangle = -i\theta(t) \sum_q \left\langle \vec{r} \right| e^{-i\omega_q t/\hbar} \left| \psi_{\mathbf{q}} \right\rangle \langle \psi_{\mathbf{q}} | \vec{r} \rangle \tag{C.4}$$

and thus

$$G^{\rm ret}(\vec{r},\vec{r},\omega)=\sum\frac{|\psi_{\mathbf{q}}(\vec{r})|^2}{\omega-\omega_q+i\delta} \tag{C.5}$$

$$N_S\left(\vec{r},\omega\right)=\sum_q|\psi_{\mathbf{q}}(\vec{r})|^2\delta(\omega-\omega_q). \tag{C.6}$$

In a perfect crystal where the $\psi_q(\vec{r})$'s are Bloch states, $|\psi_q(\vec{r})|^2=1$, and the LDOS $N_s\left(\vec{r},\omega\right)$ depends only on the energy ω. When there are impurities or defects in the system, scattering off the impurities results in the interference between the outgoing and the backscattered waves, which leads to spatial modulations in the LDOS and the topography map.

The first STM images of the wavelike features on the metallic surfaces were carried out in Eigler's group at IBM [130]. In cuprate superconductors, the analysis of the energy-dependent Fourier transformed LDOS (FT-LDOS) of $Bi_2Sr_2CaCu_2O_{8+\delta}$ single crystals [95, 97, 272, 99] based on the quasiparticle interference model has yielded segments of the Fermi surface and energy gap $\Delta_d(\vec{k})$ consistent with results of the angular-resolved photoemission spectroscopy [95, 97, 274]. Furthermore, detailed examination of the FT-LDOS has revealed a charge order coexisting with superconductivity below T_c in $Bi_2Sr_2CaCu_2O_{8+\delta}$ [257, 258, 256, 101, 73], and the charge order was demonstrated to survive well above T_c [99], as shown in §6.3. In the following paragraph, the theoretical formalism for computing the LDOS is summarized.

In the presence of an impurity potential $\mathcal{H}_{\rm imp}$, we use perturbation expansion to calculate the LDOS, *i.e.*, the imaginary part of the retarded Green's function. Define $\mathcal{G}$ as the total thermal Green's function associated with the total Hamiltonian $\mathcal{H}=\mathcal{H}_0+\mathcal{H}_{\rm imp}$ and $\mathcal{G}_0$ the unperturbed thermal Green's function associated with the Hamiltonian of a perfect crystal $\mathcal{H}_0$. Dyson's equation reads, in the operator notation,

$$\mathcal{G}=\mathcal{G}_0+\mathcal{G}_0\mathcal{H}_{\rm imp}\mathcal{G}=\mathcal{G}_0+\mathcal{G}_0\mathcal{H}_{\rm imp}\mathcal{G}_0+\mathcal{G}_0\mathcal{H}_{\rm imp}\mathcal{G}_0\mathcal{H}_{\rm imp}\mathcal{G}_0+... \tag{C.7}$$

(C.7) can be further rearranged into

$$\mathcal{G} = \mathcal{G}_0 + \mathcal{G}_0(\mathcal{H}_{\rm imp} + \mathcal{G}_0\mathcal{H}_{\rm imp}\mathcal{G}_0 + ...)\mathcal{G}_0 = \mathcal{G}_0 + \mathcal{G}_0 T \mathcal{G}_0. \tag{C.8}$$

When the impurity potential is weak, the first order T-matrix expansion is generally sufficient. Thus,

$$\mathcal{G} \approx \mathcal{G}_0 + \mathcal{G}_0\mathcal{H}_{\rm imp}\mathcal{G}_0, \tag{C.9}$$

which is the familiar Born approximation. In the real-space representation, (C.9) reads

$$\mathcal{G}(\vec{r}, \vec{r}, i\omega) \approx \mathcal{G}_0(\vec{r}, \vec{r}, i\omega) + \int d^2\vec{r_1}\mathcal{G}_0(\vec{r}, \vec{r_1}, i\omega)\mathcal{H}_{\rm imp}(\vec{r_1})\mathcal{G}_0(\vec{r_1}, \vec{r}, i\omega), \tag{C.10}$$

where $i\omega$ is the Matsubara frequency. The thermal Green's function $\mathcal{G}(\vec{r}, \vec{r}, i\omega)$ is analytically continued in the upper half of the complex ω plane ($i\omega \rightarrow \omega + i\delta$) to determine the finite-temperature retarded Green's function $\mathcal{G}^{\rm ret}(\vec{r}, \vec{r}, \omega)$. The Fourier transform of $\mathcal{G}^{\rm ret}(\vec{r}, \vec{r}, \omega)$ in turn gives us the energy-dependent FT-LDOS.

At very low temperatures, we can avoid the use of thermal Green's functions and derive similar results from Dyson's equation of the zero-temperature Green's function $G(\vec{r}, \vec{r}, \omega)$. The imaginary part of $G(\vec{r}, \vec{r}, \omega)$ is related to that of the zero-temperature retarded Green's function $G^{\rm ret}(\vec{r}, \vec{r}, \omega)$ by

$$\text{Im } [G(\vec{r}, \vec{r}, \omega)] = sgn(\omega) \text{ Im } [G^{\rm ret}(\vec{r}, \vec{r}, \omega)], \tag{C.11}$$

from which the FT-LDOS in §6.3 is deduced.